



CHORUS

This is the accepted manuscript made available via CHORUS. The article has been published as:

Temperature-induced inversion of the spin-photogalvanic effect in WTe_2 and MoTe_2

Sejoon Lim, Catherine R. Rajamathi, Vicky Süß, Claudia Felser, and Aharon Kapitulnik

Phys. Rev. B **98**, 121301 — Published 10 September 2018

DOI: [10.1103/PhysRevB.98.121301](https://doi.org/10.1103/PhysRevB.98.121301)

Temperature-Induced Inversion of the Spin-Photogalvanic Effect in WTe_2 and MoTe_2

Sejoon Lim,^{1,2} Catherine R. Rajamathi,³ Vicky Süß,³ Claudia Felser,³ and Aharon Kapitulnik^{1,2,4}

¹*Department of Applied Physics, Stanford University, Stanford, California 94305, USA*

²*Stanford Institute for Materials and Energy Sciences, SLAC National Accelerator Laboratory, 2575 Sand Hill Road, Menlo Park, California 94025, USA*

³*Max Planck Institute for Chemical Physics of Solids, 01187 Dresden, Germany*

⁴*Department of Physics, Stanford University, Stanford, California 94305, USA*

(Dated: July 24, 2018)

We investigate the generation and temperature-induced evolution of optically-driven spin photocurrents in WTe_2 and MoTe_2 . By correlating the scattering-plane dependence of the spin photocurrents with the symmetry analysis, we find that a sizeable spin photocurrent can be controllably driven along the chain direction by optically exciting the system in the high-symmetry y - z plane. Temperature dependence measurements show that pronounced variations in the spin photocurrent emerge at temperatures that coincide with the onset of anomalies in their transport and optical properties. The decreasing trend in the temperature dependence starting below ~ 150 K is attributed to the temperature-induced Lifshitz transition. The sign inversion of the spin photocurrent, observed around 50 K in WTe_2 and around 120 K in MoTe_2 , may have its origin in an interaction that involves multiple kinds of carriers.

In recent years, the semimetallic transition-metal dichalcogenides, WTe_2 and MoTe_2 , have provided a platform for realizing unusual physical phenomena, including the nonsaturating extremely large magnetoresistance^{1,2}, the pressure-induced enhancement of superconductivity³⁻⁵, and the type-II Weyl semimetal states⁶⁻¹⁶. Extensive research has been directed at uncovering the physical mechanisms that lead to these properties and their relation to the topological nature of the Weyl nodes. In the process, both compounds have been revealed to be governed by a complicated electronic structure that is characterized by an anomalous temperature dependence.

In the case of WTe_2 , for example, angle-resolved photoemission spectroscopy showed that compensation between electron and hole densities observed at low temperatures rapidly breaks down with increasing temperature^{17,18}, and this shift of the Fermi level leads to a Lifshitz transition, suppressing the hole pockets above ~ 160 K¹⁸. The magnetotransport study found a pronounced enhancement of both the effective mass anisotropy and the magnetoresistance below ~ 75 K, which suggests yet another possible change in the electronic structure¹⁹. Hall and thermoelectric transport studies observed significant changes in the Hall coefficient below ~ 50 K^{20,21} and sign inversion of the thermoelectric power around 60 K²², respectively. Additional evidence for the change in the electronic structure around 50 K was provided by an ultrafast transient reflectivity measurement, which revealed an unusual decrease in the time scale of a relaxation process that was attributed to phonon-assisted electron-hole recombination²³.

Further enriched with spin-splitting of bands due to strong spin-orbit coupling and broken inversion symmetry as illustrated in Fig. 1, spin-photogalvanics^{25,26}, in which optical orientation with circularly polarized radiation leads to a spin-polarized electric current via the circular photogalvanic and the spin-galvanic effects,

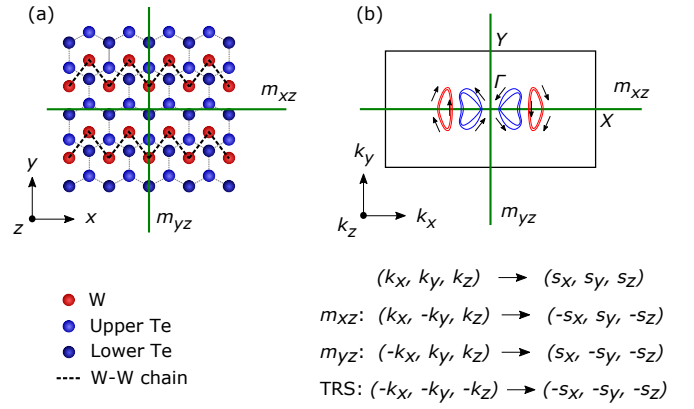


FIG. 1 (color online). (a) Top schematic view of the crystal structure of a single Te-W-Te compound layer in WTe_2 (space group $Pmn2_1$). The green lines, labeled m_{xz} and m_{yz} , represent the glide reflection symmetry in the x - z plane and the mirror symmetry in the y - z plane, respectively. (b) Schematics of the Fermi surface and its spin texture in the $k_z = 0$ plane of the Brillouin zone, adopted from previous spin- and angle-resolved photoemission studies^{9,24}. The red and blue lines indicate the electron and hole pockets, respectively. The black arrows indicate their spin texture, which necessarily respects m_{xz} , m_{yz} , and TRS, simultaneously. Effects of the symmetry operations on spins are summarized.

may provide insight into temperature-dependent dynamic properties of spin-polarized carriers in these compounds. Previously, this technique has been applied to study point group symmetries and dynamic properties of helicity-dependent carriers in semiconductors²⁷, quantum well structures²⁵, topological insulators²⁸⁻³⁰, semiconducting transition-metal dichalcogenides³¹, and recently type-I Weyl semimetals³²⁻³⁵.

In this Letter, we report a detailed study of the generation and temperature-induced evolution of optically-driven spin photocurrents in WTe_2 and MoTe_2 . We first

show, by varying the direction of exciting radiation, that the mirror symmetries along with time-reversal symmetry (TRS) forbid the generation of a spin photocurrent under certain experimental geometries. Its correlation with the symmetry analysis suggests that the generating mechanisms are rooted in the electronic structure and its spin texture, which necessarily respect the crystal symmetries. Subsequent temperature dependence measurements reveal sign inversion of the spin photocurrent around 50 K in WTe₂ and around 120 K in MoTe₂. Along with the trend in the temperature dependence, which features a drop in the photocurrent magnitude starting below the Lifshitz transition temperature around 150 K, these observations suggest that the anomalous temperature dependence of the spin photocurrent in these compounds may be associated with the temperature-induced evolution of their electronic structure.

We first distinguish the photocurrent response that arises from the photogalvanic effects from the photoinduced thermoelectric response³⁰. Figures 2(a) and 2(b) show the variation of the electric current, induced along the x axis of WTe₂, as the obliquely incident p -polarized light in the y - z plane is scanned across the contacts at room temperature³⁶. The observation of the current flow away from the heated contacts, which is consistent with the n -type thermoelectric behavior of WTe₂ at room temperature²², along with the reversal of the current direction upon sweeping the light across the contacts, indicates the presence of a large thermoelectric contribution in the photoinduced electric current. As shown in the polarization dependence measurements in Fig. 2(c), however, this thermoelectric contribution is mostly independent of the polarization of incident radiation, which allows us to selectively investigate the photocurrent response by analyzing its polarization dependence. This analysis is further supported by the observation of the same n -type thermoelectric behavior, yet a sign-flipped spin photocurrent, upon rotating the y - z scattering plane by 180° about the z axis, as shown in Fig. 2(d).

The observed polarization dependence can be described by a phenomenological expression, given by

$$\begin{aligned} j_\lambda = & \sum_{\mu\nu} \chi_{\lambda\mu\nu} \frac{(E_\mu E_\nu^* + E_\nu E_\mu^*)}{2} + \sum_{\mu} \gamma_{\lambda\mu} i (\mathbf{E} \times \mathbf{E}^*)_{\mu} \\ & + \sum_{\mu} Q_{\lambda\mu} S_{\mu} + \sum_{\delta\mu\nu} T_{\lambda\delta\mu\nu} q_{\delta} E_{\mu} E_{\nu}^*, \end{aligned} \quad (1)$$

where \mathbf{E} is the complex amplitude of the electric field of incident radiation, \mathbf{q} is its wavevector inside the crystal, and \mathbf{S} is the nonequilibrium average spin polarization²⁵. The set of symmetry elements contained in the point group C_{2v} of WTe₂ is encoded in the tensors, $\chi_{\lambda\mu\nu}$, $\gamma_{\lambda\mu}$, $Q_{\lambda\mu}$, and $T_{\lambda\delta\mu\nu}$, which describe the linear and circular photogalvanic, the spin-galvanic, and the photon drag effects, respectively. In terms of the phase angle φ between the polarization axis of the laser radiation and the optical axis of the $\lambda/4$ plate, the photocurrent can be expressed as $j_x = j_C \sin 2\varphi + j_{L1} \sin 4\varphi + j_{L2} \cos 4\varphi + j_0$ with four

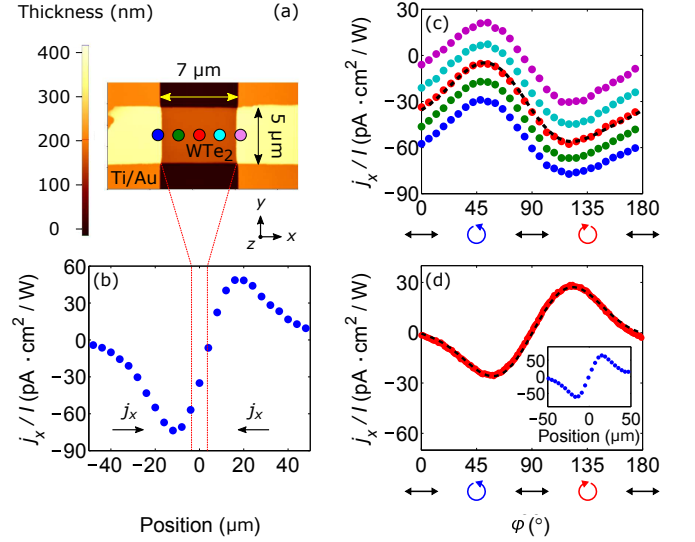


FIG. 2 (color online). (a) Atomic force microscopy image of the measured 160 nm thick flake of WTe₂. (b) Variation of the photoinduced electric current j_x , normalized by the light intensity I , as the obliquely incident p -polarized light in the y - z plane is scanned across the contacts at room temperature. (c) Phase angle dependence of j_x/I . Each colored plot represents a measurement carried out with the incident radiation centered at the corresponding location shown in (a). The dashed black line represents a fit to the phenomenological expression. (d) Same measurements as (b) and (c), but with the y - z scattering plane rotated by 180° about the z axis.

scaling parameters, where the first term, which is proportional to the helicity $P_{circ} = \sin 2\varphi \propto |\mathbf{E} \times \mathbf{E}^*| \propto |\mathbf{S}|$, mainly arises from the circular photogalvanic and the spin-galvanic effects. In this study, we restrict our attention to these spin-related photogalvanic effects, which are parametrized by a single scaling parameter j_C .

Below, we investigate how the mirror and time-reversal symmetries of WTe₂ allow only the transverse spin photocurrent when the light is incident in the high-symmetry x - z or y - z plane using spin-selective optical excitation as the generating mechanism of spin photocurrents. Analogous data on MoTe₂ can be found in the Supplemental Material³⁶.

Figure 3 shows the photocurrent measured at room temperature under three different experimental geometries. When the light is incident in the y - z plane, a large spin photocurrent develops along the x axis, as shown in Fig. 3(a). In contrast, this spin photocurrent significantly diminishes, as shown in Fig. 3(b), when the scattering plane is rotated into the x - z plane. On a microscopic level, these observations indicate that an asymmetric distribution of photoexcited carriers is induced predominantly about the high-symmetry scattering plane in k space as a result of optical orientation^{25,26}.

To understand this asymmetric photoexcitation, we note that each k point in the Brillouin zone of WTe₂ is related to seven other points by the mirror and time-

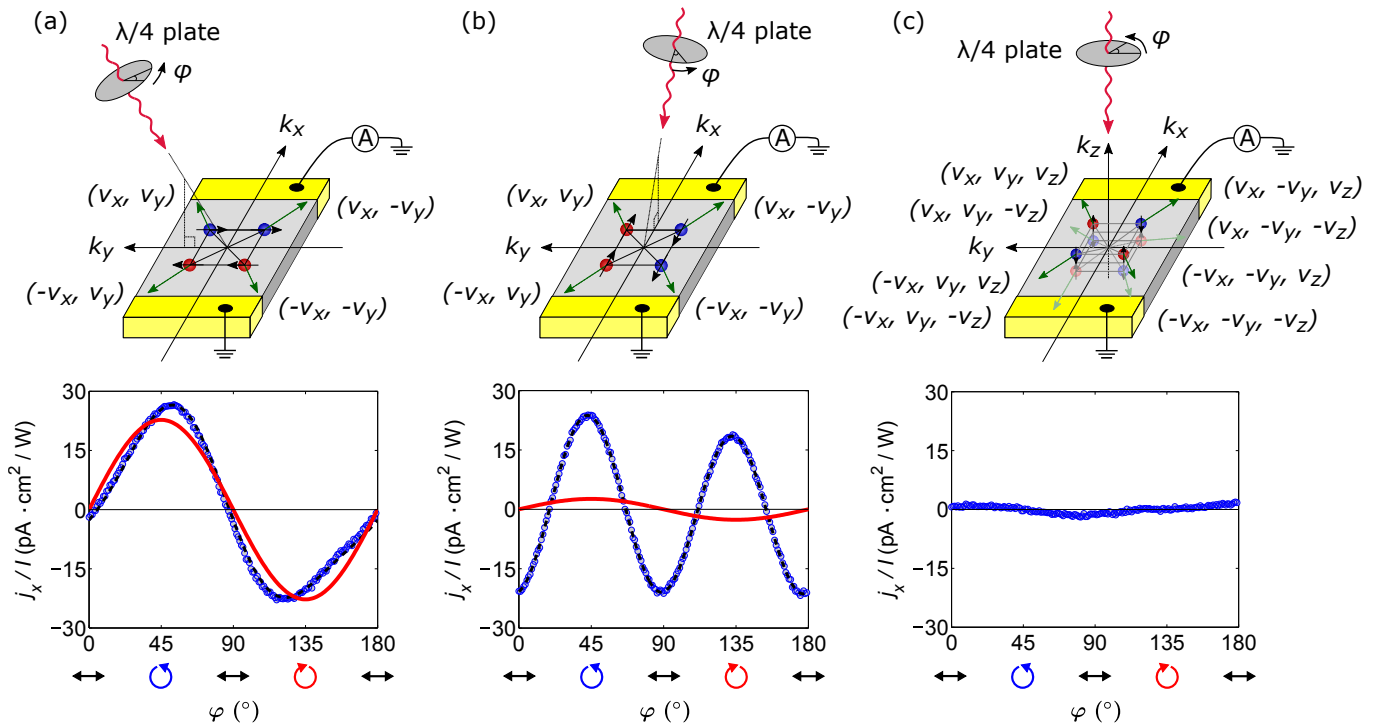


FIG. 3 (color online). (a) Sketch of the experimental geometry and the phase angle dependence of j_x/I in WTe_2 with the light obliquely incident in the y - z plane at an angle of 40° . In the schematic, the four symmetry-related states in the $k_z = 0$ plane are shown with their spins marked with black arrows. The blue and red fillings indicate those that are preferentially excited with right- and left-handed helicity, respectively. Their group velocities are indicated by long green arrows and described on the sides. In the data figure, the open blue circles represent the photocurrent j_x/I measured at room temperature with the polarization-independent component removed. The dashed black line shows a fit to the phenomenological expression. The solid red line is the extracted spin-dependent component, which is proportional to P_{circ} . (b) Same as (a), but with the light obliquely incident in the x - z plane. (c) Same as (a), but with the light normally incident.

reversal symmetries, whose constraints on the spin texture are described in Fig. 1(b). For simplicity, we consider here the k points lying in the $k_z = 0$ plane of the Brillouin zone, which have only in-plane spin components and four symmetry-related states. As illustrated in the sketches in Figs. 3(a) and 3(b), depending on its helicity, the incident circularly polarized radiation excites the occupied states asymmetrically about the scattering plane. In contrast, photoexcitation is symmetric about the other high-symmetry plane, which results in a net spin-polarized photocurrent in the direction normal to the scattering plane. This analysis, based on crystal symmetries, can also account for the absence of a spin photocurrent under normal incidence, which is described in Fig. 3(c). It is also applicable when k -dependent spin-flip scattering of photoexcited carriers, instead of spin-selective photoexcitation, is considered as the generating mechanism of spin photocurrents.

Having identified the electronic structure and its spin texture as the bases for determining the properties of spin photocurrents, we proceed to investigate how the spin photocurrent in WTe_2 evolves as its electronic structure undergoes transitions with temperature. Figure 4 shows this temperature-induced evolution, quantified by

the scaling parameter j_C . As shown in the lower inset, our light intensity of $\sim 42 \text{ W/cm}^2$ lies in the range where the spin photocurrent scales linearly with the intensity, which signals that contributions from higher-order nonlinear effects are small. Above $\sim 150 \text{ K}$, the spin photocurrent stays relatively constant, which likely indicates that the transition probabilities and the momentum and spin relaxation times are not strongly affected by the Fermi level shift and thermal broadening in this temperature range. As temperature is lowered below $\sim 150 \text{ K}$, the spin photocurrent starts to decrease and this decreasing behavior accelerates. Intriguingly, this onset roughly coincides with the Lifshitz transition around 160 K , below which the hole bands begin to surface above the Fermi level, as schematically illustrated in the upper inset of Fig. 4. This coincidence suggests that the hole pockets may play a role in generating and scattering the photoexcited carriers.

One possible mechanism is through an enhancement of interband relaxation of the photoexcited carriers. As the number of holes increases with the appearance of the hole pockets in the Fermi surface, both the radiative and non-radiative phonon-assisted recombination processes become more efficient, which facilitates interband cooling²³.

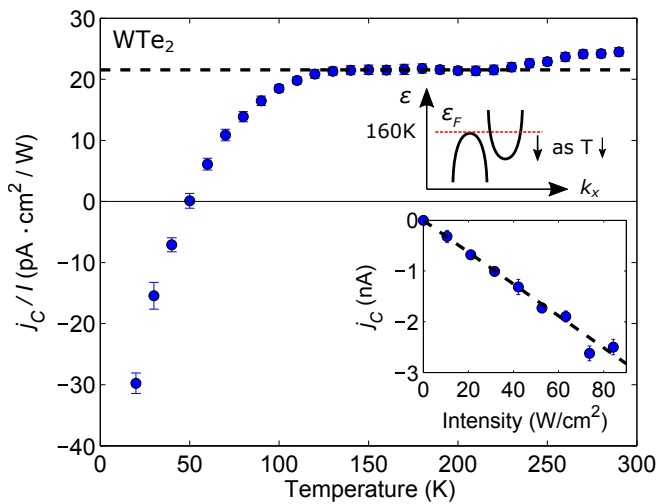


FIG. 4 (color online). Temperature dependence of the scaling parameter j_C in WTe_2 . The horizontal dashed black line has been added as a guide to the eyes. The lower inset shows its intensity dependence at 20 K. The dashed black line in the inset represents a linear fit. The upper inset shows a schematic of the band structure along Γ - X . Around 160 K, the Fermi level, represented by the dashed red line, crosses the top of the hole band.

The resulting drive to restore the nonequilibrium carrier distribution back to equilibrium would then tend to increase the probability rates for optical transitions and decrease the momentum and spin relaxation times, thereby influencing both the circular photogalvanic and the spin-galvanic processes^{25,26}.

Upon lowering the temperature further, the sign of the scaling parameter j_C flips around 50 K, which indicates that the net spin photocurrent reverses its direction of flow. Such inversion at fixed helicity has frequently been observed in spectral responses, where variations of the photon energy shift optical transitions across band minima^{41–43}. In contrast, temperature-induced sign inversion has been rarely demonstrated⁴⁴. Its observation in p -GaAs/AlGaAs quantum wells⁴⁴ has been attributed to a change of the scattering mechanism from phonons to impurities; however, it may have a different origin in the case of WTe_2 , because the onset temperature is high. Based on the aforementioned transport and optical studies pointing toward a possible change in the electronic structure around 50 K and a plausible explanation for the temperature dependence of the Hall coefficient and the thermoelectric power given by a three-carrier model²², it may be likely that this inversion arises from an interaction that involves multiple kinds of carriers.

As shown in Fig. 5, similar sign inversion is observed in MoTe_2 around 120 K, which again coincides with the temperature below which its thermoelectric power crosses over to a p -type behavior^{2,45}. In contrast to WTe_2 , however, this temperature range is higher than the onset temperature, around 70 K, of other anomalies present

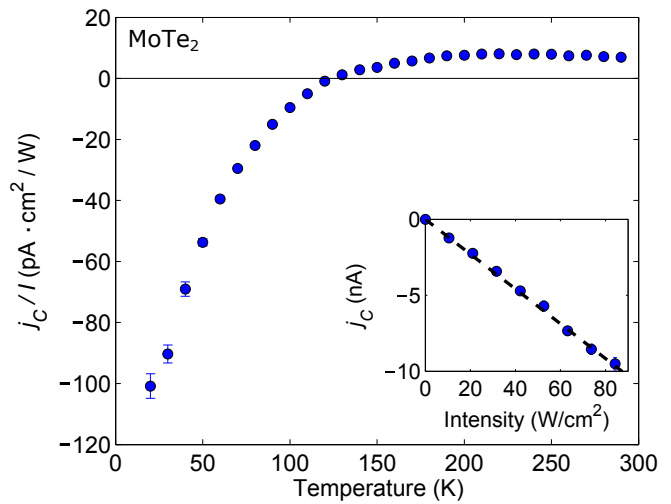


FIG. 5 (color online). Temperature dependence of the scaling parameter j_C in MoTe_2 . The inset shows its linear intensity dependence at 20 K.

in MoTe_2 , such as in the effective mass anisotropy⁴⁵, the magnetoresistance⁴⁵, the Hall coefficient^{2,45,46}, and the specific heat², which suggests that the multiple-carrier picture may have the dominant effect. The decreasing trend of the scaling parameter j_C below ~ 150 K may again be associated with a possible Lifshitz transition, which was suggested by previous Hall and thermoelectric transport studies⁴⁵, although the onset is not as sharp as in WTe_2 possibly due to the substantial thermal hysteresis associated with the structural transition, which extends from ~ 125 K to room temperature^{2,47}. We also note that the spin photocurrent is small but nonzero above ~ 250 K, where MoTe_2 is known to crystallize in the centrosymmetric $17'$ phase^{11,47,48}. We believe that this contribution arises from the surface layers, which necessarily break inversion symmetry.

In summary, we find pronounced temperature-induced variations of the optically-driven spin photocurrents in WTe_2 and MoTe_2 , whose origin may be associated with anomalies in their transport and optical properties. In particular, we showed that sign inversion at fixed helicity can be induced by varying the temperature. Its rough overlap in temperature with the n -type to p -type crossover in the thermoelectric power in both compounds supports microscopic mechanisms based on a multiple-carrier picture. However, due to the numerous other anomalies that emerge at nearby temperatures, a detailed understanding of their correlation may be crucial in elucidating the exact origin of the sign inversion.

This work was supported by the Department of Energy, Office of Science, Basic Energy Sciences, Materials Sciences and Engineering Division, under Contract DE-AC02-76SF00515. Part of this work was performed at the Stanford Nano Shared Facilities with support from the Gordon and Betty Moore Foundation's EPiQS Initiative through Grant GBMF4529.

-
- ¹ M. N. Ali, J. Xiong, S. Flynn, J. Tao, Q. D. Gibson, L. M. Schoop, T. Liang, N. Haldolaarachchige, M. Hirschberger, N. P. Ong, and R. J. Cava, *Nature (London)* **514**, 205 (2014).
- ² D. Rhodes, R. Schönemann, N. Aryal, Q. Zhou, Q. R. Zhang, E. Kampert, Y.-C. Chiu, Y. Lai, Y. Shimura, G. T. McCandless, J. Y. Chan, D. W. Paley, J. Lee, A. D. Finke, J. P. C. Ruff, S. Das, E. Manousakis, and L. Balicas, *Phys. Rev. B* **96**, 165134 (2017).
- ³ D. Kang, Y. Zhou, W. Yi, C. Yang, J. Guo, Y. Shi, S. Zhang, Z. Wang, C. Zhang, S. Jiang, A. Li, K. Yang, Q. Wu, G. Zhang, L. Sun, and Z. Zhao, *Nat. Commun.* **6**, 7804 (2015).
- ⁴ X.-C. Pan, X. Chen, H. Liu, Y. Feng, Z. Wei, Y. Zhou, Z. Chi, L. Pi, F. Yen, F. Song, X. Wan, Z. Yang, B. Wang, G. Wang, and Y. Zhang, *Nat. Commun.* **6**, 7805 (2015).
- ⁵ Y. Qi, P. G. Naumov, M. N. Ali, C. R. Rajamathi, W. Schnelle, O. Barkalov, M. Hanfland, S.-C. Wu, C. Shekhar, Y. Sun, V. Süß, M. Schmidt, U. Schwarz, E. Pippel, P. Werner, R. Hillebrand, T. Förster, E. Kampert, S. Parkin, R. J. Cava, C. Felser, B. Yan, and S. A. Medvedev, *Nat. Commun.* **7**, 11038 (2016).
- ⁶ A. A. Soluyanov, D. Gresch, Z. Wang, Q. Wu, M. Troyer, X. Dai, and B. A. Bernevig, *Nature (London)* **527**, 495 (2015).
- ⁷ F. Y. Bruno, A. Tamai, Q. S. Wu, I. Cucchi, C. Barreateau, A. de la Torre, S. M. Walker, S. Riccò, Z. Wang, T. K. Kim, M. Hoesch, M. Shi, N. C. Plumb, E. Giannini, A. A. Soluyanov, and F. Baumberger, *Phys. Rev. B* **94**, 121112 (2016).
- ⁸ Y. Wu, D. Mou, N. H. Jo, K. Sun, L. Huang, S. L. Bud'ko, P. C. Canfield, and A. Kaminski, *Phys. Rev. B* **94**, 121113 (2016).
- ⁹ B. Feng, Y.-H. Chan, Y. Feng, R.-Y. Liu, M.-Y. Chou, K. Kuroda, K. Yaji, A. Harasawa, P. Moras, A. Barinov, W. Malaeb, C. Bareille, T. Kondo, S. Shin, F. Komori, T.-C. Chiang, Y. Shi, and I. Matsuda, *Phys. Rev. B* **94**, 195134 (2016).
- ¹⁰ C. Wang, Y. Zhang, J. Huang, S. Nie, G. Liu, A. Liang, Y. Zhang, B. Shen, J. Liu, C. Hu, Y. Ding, D. Liu, Y. Hu, S. He, L. Zhao, L. Yu, J. Hu, J. Wei, Z. Mao, Y. Shi, X. Jia, F. Zhang, S. Zhang, F. Yang, Z. Wang, Q. Peng, H. Weng, X. Dai, Z. Fang, Z. Xu, C. Chen, and X. J. Zhou, *Phys. Rev. B* **94**, 241119 (2016).
- ¹¹ Y. Sun, S.-C. Wu, M. N. Ali, C. Felser, and B. Yan, *Phys. Rev. B* **92**, 161107 (2015).
- ¹² Z. Wang, D. Gresch, A. A. Soluyanov, W. Xie, S. Kushwaha, X. Dai, M. Troyer, R. J. Cava, and B. A. Bernevig, *Phys. Rev. Lett.* **117**, 056805 (2016).
- ¹³ L. Huang, T. M. McCormick, M. Ochi, Z. Zhao, M.-T. Suzuki, R. Arita, Y. Wu, D. Mou, H. Cao, J. Yan, N. Trivedi, and A. Kaminski, *Nat. Mater.* **15**, 1155 (2016).
- ¹⁴ K. Deng, G. Wan, P. Deng, K. Zhang, S. Ding, E. Wang, M. Yan, H. Huang, H. Zhang, Z. Xu, J. Denlinger, A. Fedorov, H. Yang, W. Duan, H. Yao, Y. Wu, S. Fan, H. Zhang, X. Chen, and S. Zhou, *Nat. Phys.* **12**, 1105 (2016).
- ¹⁵ J. Jiang, Z. K. Liu, Y. Sun, H. F. Yang, C. R. Rajamathi, Y. P. Qi, L. X. Yang, C. Chen, H. Peng, C.-C. Hwang, S. Z. Sun, S.-K. Mo, I. Vobornik, J. Fujii, S. S. P. Parkin, C. Felser, B. H. Yan, and Y. L. Chen, *Nat. Commun.* **8**, 13973 (2017).
- ¹⁶ A. Tamai, Q. S. Wu, I. Cucchi, F. Y. Bruno, S. Riccò, T. K. Kim, M. Hoesch, C. Barreateau, E. Giannini, C. Besnard, A. A. Soluyanov, and F. Baumberger, *Phys. Rev. X* **6**, 031021 (2016).
- ¹⁷ I. Pletikosić, M. N. Ali, A. V. Fedorov, R. J. Cava, and T. Valla, *Phys. Rev. Lett.* **113**, 216601 (2014).
- ¹⁸ Y. Wu, N. H. Jo, M. Ochi, L. Huang, D. Mou, S. L. Bud'ko, P. C. Canfield, N. Trivedi, R. Arita, and A. Kaminski, *Phys. Rev. Lett.* **115**, 166602 (2015).
- ¹⁹ L. R. Thoutam, Y. L. Wang, Z. L. Xiao, S. Das, A. Luican-Mayer, R. Divan, G. W. Crabtree, and W. K. Kwok, *Phys. Rev. Lett.* **115**, 046602 (2015).
- ²⁰ Y. Luo, H. Li, Y. M. Dai, H. Miao, Y. G. Shi, H. Ding, A. J. Taylor, D. A. Yarotski, R. P. Prasankumar, and J. D. Thompson, *Appl. Phys. Lett.* **107**, 182411 (2015).
- ²¹ Y. L. Wang, L. R. Thoutam, Z. L. Xiao, J. Hu, S. Das, Z. Q. Mao, J. Wei, R. Divan, A. Luican-Mayer, G. W. Crabtree, and W. K. Kwok, *Phys. Rev. B* **92**, 180402 (2015).
- ²² S. Kabashima, *J. Phys. Soc. Jpn.* **21**, 945 (1966).
- ²³ Y. M. Dai, J. Bowlan, H. Li, H. Miao, S. F. Wu, W. D. Kong, P. Richard, Y. G. Shi, S. A. Trugman, J.-X. Zhu, H. Ding, A. J. Taylor, D. A. Yarotski, and R. P. Prasankumar, *Phys. Rev. B* **92**, 161104 (2015).
- ²⁴ J. Jiang, F. Tang, X. C. Pan, H. M. Liu, X. H. Niu, Y. X. Wang, D. F. Xu, H. F. Yang, B. P. Xie, F. Q. Song, P. Dudin, T. K. Kim, M. Hoesch, P. K. Das, I. Vobornik, X. G. Wan, and D. L. Feng, *Phys. Rev. Lett.* **115**, 166601 (2015).
- ²⁵ S. D. Ganichev and W. Prettl, *J. Phys. Condens. Matter* **15**, R935 (2003).
- ²⁶ E. L. Ivchenko and S. D. Ganichev, arXiv:1710.09223.
- ²⁷ V. I. Belinicher and B. I. Sturman, *Usp. Fiz. Nauk* **130**, 415 (1980).
- ²⁸ J. E. Moore and J. Orenstein, *Phys. Rev. Lett.* **105**, 026805 (2010).
- ²⁹ P. Hosur, *Phys. Rev. B* **83**, 035309 (2011).
- ³⁰ J. W. McIver, D. Hsieh, H. Steinberg, P. Jarillo-Herrero, and N. Gedik, *Nat. Nanotechnol.* **7**, 96 (2012).
- ³¹ H. Yuan, X. Wang, B. Lian, H. Zhang, X. Fang, B. Shen, G. Xu, Y. Xu, S.-C. Zhang, H. Y. Hwang, and Y. Cui, *Nat. Nanotechnol.* **9**, 851 (2014).
- ³² H. Ishizuka, T. Hayata, M. Ueda, and N. Nagaosa, *Phys. Rev. Lett.* **117**, 216601 (2016).
- ³³ C.-K. Chan, N. H. Lindner, G. Refael, and P. A. Lee, *Phys. Rev. B* **95**, 041104 (2017).
- ³⁴ F. de Juan, A. G. Grushin, T. Morimoto, and J. E. Moore, *Nat. Commun.* **8**, 15995 (2017).
- ³⁵ Q. Ma, S.-Y. Xu, C.-K. Chan, C.-L. Zhang, G. Chang, Y. Lin, W. Xie, T. Palacios, H. Lin, S. Jia, P. A. Lee, P. Jarillo-Herrero, and N. Gedik, *Nat. Phys.* **13**, 842 (2017).
- ³⁶ See Supplemental Material for details on the crystal growth, the experimental setup, the determination of the crystal axes, and the scattering-plane dependence of the spin photocurrent in MoTe₂, which includes Refs. [11, 25, 37-40].
- ³⁷ A. J. Frenzel, C. C. Homes, Q. D. Gibson, Y. M. Shao, K. W. Post, A. Charnukha, R. J. Cava, and D. N. Basov, *Phys. Rev. B* **95**, 245140 (2017).

- ³⁸ C. C. Homes, M. N. Ali, and R. J. Cava, *Phys. Rev. B* **92**, 161109 (2015).
- ³⁹ Q. Song, X. Pan, H. Wang, K. Zhang, Q. Tan, P. Li, Y. Wan, Y. Wang, X. Xu, M. Lin, X. Wan, F. Song, and L. Dai, *Sci. Rep.* **6**, 29254 (2016).
- ⁴⁰ Q. Song, H. Wang, X. Pan, X. Xu, Y. Wang, Y. Li, F. Song, X. Wan, Y. Ye, and L. Dai, *Sci. Rep.* **7**, 1758 (2017).
- ⁴¹ S. D. Ganichev, V. V. Bel'kov, P. Schneider, E. L. Ivchenko, S. A. Tarasenko, W. Wegscheider, D. Weiss, D. Schuh, E. V. Berezulin, and W. Prettl, *Phys. Rev. B* **68**, 035319 (2003).
- ⁴² L. E. Golub, *Phys. Rev. B* **67**, 235320 (2003).
- ⁴³ C. L. Yang, H. T. He, L. Ding, L. J. Cui, Y. P. Zeng, J. N. Wang, and W. K. Ge, *Phys. Rev. Lett.* **96**, 186605 (2006).
- ⁴⁴ S. D. Ganichev, H. Ketterl, W. Prettl, E. L. Ivchenko, and L. E. Vorobjev, *Appl. Phys. Lett.* **77**, 3146 (2000).
- ⁴⁵ F. C. Chen, H. Y. Lv, X. Luo, W. J. Lu, Q. L. Pei, G. T. Lin, Y. Y. Han, X. B. Zhu, W. H. Song, and Y. P. Sun, *Phys. Rev. B* **94**, 235154 (2016).
- ⁴⁶ Q. Zhou, D. Rhodes, Q. R. Zhang, S. Tang, R. Schönemann, and L. Balicas, *Phys. Rev. B* **94**, 121101 (2016).
- ⁴⁷ R. Clarke, E. Marseglia, and H. P. Hughes, *Philos. Mag. B* **38**, 121 (1978).
- ⁴⁸ H. Sakai, K. Ikeura, M. S. Bahramy, N. Ogawa, D. Hashizume, J. Fujioka, Y. Tokura, and S. Ishiwata, *Sci. Adv.* **2**, e1601378 (2016).